Dynamics and Heat Transfer Associated With a Single Bubble During Nucleate Boiling on a Horizontal Surface

G. Son

V. K. Dhir
Mem. ASME

N. Ramanujapu

Mechanical and Aerospace Engineering Department, University of California, Los Angeles, CA 90095

In this study, a complete numerical simulation of a growing and departing bubble on a horizontal surface has been performed. A finite difference scheme is used to solve the equations governing conservation of mass, momentum, and energy in the vapor-liquid layers. The vapor-liquid interface is captured by a level set method which is modified to include the influence of phase change at the liquid-vapor interphase. The disjoining pressure effect is included in the numerical analysis to account for heat transfer through the liquid microlayer. From the numerical simulation, the location where the vapor-liquid interface contacts the wall is observed to expand and then retract as the bubble grows and departs. The effect of static contact angle and wall superheat on bubble dynamics has been quantified. The bubble growth predicted from numerical analysis has been found to compare well with the experimental data reported in the literature and that obtained in this work.

Introduction

Nucleate boiling is a liquid-vapor phase-change process associated with bubble formation. As it is a very efficient mode of heat transfer, the boiling process has been studied extensively during the last half century. Although significant progress has been made in modeling the nucleate boiling process, a mechanistic model to describe the phenomena and predict the heat transfer coefficients without employing empirical constants has not yet been developed for isolated bubble regime (partial nucleate boiling) on a horizontal surface. In most previous studies, modeling of bubble dynamics including the growth and departure of the bubble has been overly simplified and the flow and temperature fields influenced by the bubble motion have not been correctly treated.

Fritz (1935) was the first to develop a criterion for bubble departure by balancing buoyancy with surface tension forces acting on a static bubble. He proposed an empirical expression for the bubble departure diameter as

$$D_d = 0.0208\varphi\sqrt{\sigma/g(\rho_l - \rho_v)} \tag{1}$$

where the contact angle φ is measured in degrees. Although deviations of predictions made from Eq. (1) with the data for the bubble diameter at departure reported in the literature have been observed, Eq. (1) provides an appropriate length scale for the boiling process. Including the effect of the bubble growth velocity, Staniszewski (1959) suggested an equation for the bubble diameter at departure as

$$D_d = 0.0071\varphi\sqrt{2\sigma/g(\rho_l - \rho_v)}\left(1 + 0.435\frac{dD}{dt}\right) \tag{2}$$

where dD/dt is given in inches per second just prior to departure. This correlation was based on his experimental observation that faster growing bubbles grew bigger before departure. The criterion for bubble departure has been improved by including several other forces such as liquid inertia and drag (Hsu and Graham, 1976). However, the evaluation of these forces requires knowledge of the bubble growth rate.

An expression for the asymptotic growth of a spherical bubble placed in a superheated liquid layer of infinite extent was obtained by Plesset and Zwick (1954):

$$D = 4\sqrt{\frac{3}{\pi}}\sqrt{\alpha_l t}\frac{\rho_l c_{pl}\Delta T}{\rho_v h_{fg}}. \tag{3}$$

This expression suggests that the growth rate of a bubble is linearly proportional to liquid superheat, ΔT. However, for a bubble attached to a heater surface, the growth rate cannot be obtained analytically because the temperature field around the bubble is not uniform and the bubble shape changes continuously. Mikic et al. (1970) used a geometric factor to relate the shape of a bubble growing on the heater surface to a perfect sphere. Accounting for the thermal energy that is stored in the superheated liquid layer prior to bubble inception, they obtained an approximate solution for the bubble growth rate. Since the initial energy content of the superheated liquid layer surrounding the bubble depends on the waiting time, the model exhibits the dependence of bubble growth rate on the waiting time. However, the model did not include the evaporation from the liquid microlayer underneath the base of a bubble.

The existence of the microlayer underneath a bubble was confirmed experimentally by Cooper and Lloyd (1969) through the observation of fluctuations in the heater surface temperature. Using the lubrication theory for the liquid flow in the microlayer, they deduced the thickness of the microlayer as

$$\delta = 0.8\sqrt{\nu_l t}. \tag{4}$$

Although Cooper and Lloyd proved the importance of microlayer evaporation, they did not account for long range forces when the microlayer is very thin. Complete analysis for the microlayer including disjoining pressure, vapor recoil pressure, and interfacial heat transfer resistance has been carried out by Lay and Dhir (1995). As a result, they were able to predict the maximum diameter of vapor stems in fully developed nucleate boiling. According to their analysis, local heat fluxes as high as 1.54×10^8 W/m^2 can exist in the very thin film.

Recently, Lee and Nydahl (1989) have numerically simulated

Contributed by the Heat Transfer Division for publication in the JOURNAL OF HEAT TRANSFER. Manuscript received by the Heat Transfer Division, Aug. 2, 1998; revision received, Feb. 3, 1999. Keywords: Boiling, Bubble Growth, Heat Transfer, Multiphase, Numerical Methods. Associate Technical Editor: P. Ayyaswamy.

the bubble growth in nucleate boiling including the microlayer. For the thickness of the microlayer, they have used the formulation of Cooper and Lloyd. To match the predicted bubble growth with the experimental data reported in the literature, they reduced the lead constant in Eq. (4) to 0.55. Although Lee and Nydahl accounted for the flow field and temperature field correctly by solving the momentum and energy equations in the liquid, they had to assume that the bubble remained hemispherical in shape during its growth and as such they could not demonstrate the departure process of the bubble.

The objective of this study is to perform a complete simulation of the hydrodynamics and heat transfer associated with a single bubble, the shape of which changes continuously during the growth. Through the analysis new physical insights can be gained into partial nucleate boiling, which has eluded the simplified models developed previously. As such the equations governing conservation of mass, momentum, and energy in the vapor and liquid phases are solved numerically. The vapor-liquid interface is captured by a level set method which can easily handle breaking and merging of the interface. This method has been applied to adiabatic incompressible two-phase flow by Sussman et al. (1994) and to film boiling near critical pressures by Son and Dhir (1998). In this work, the level set formulation, modified to accommodate the liquid-vapor phase change, is applied for simulation of partial nucleate boiling on a horizontal surface.

Analysis

In analyzing the growth of a single bubble, the computational domain is divided into micro and macro regions as shown in Fig. 1. The micro region contains the thin film that forms underneath the bubble whereas the macro region consists of the bubble and the liquid surrounding the bubble. In carrying out the analysis the flows are assumed to be axisymmetric and laminar and the fluid properties including density, viscosity, and thermal conductivity are assumed to be constant in each phase. For the low-wall superheats investigated in this study, the liquid viscosity changes by less than nine percent and the other thermophysical properties change by less than three percent. Therefore, the assumption of constant property is not too restrictive so long as the computations are performed for low superheats.

Liquid Microlayer. Lubrication theory for the microlayer has been used and validated by a number of investigators in the literature (refer to Wayner (1992) and Lay and Dhir (1995)). The equation of mass conservation in the microlayer is written as

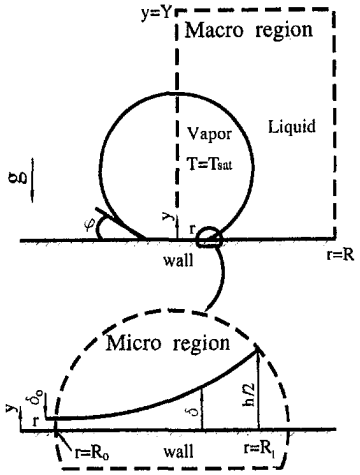

Fig. 1 Macro and micro regions used in numerical simulation

$$\frac{\partial \delta}{\partial t} = v_l - q/\rho_l h_{fg}. \tag{5}$$

In Eq. (5), the liquid velocity normal to the vapor-liquid interface, v_l, is obtained from the continuity equation as

$$v_l = -\frac{1}{r}\frac{\partial}{\partial r}\int_o^\delta r u_l dy. \tag{6}$$

The momentum equation for the microlayer is written as

$$\frac{\partial p_l}{\partial r} = \mu_l \frac{\partial^2 u_l}{\partial y^2}. \tag{7}$$

The energy conservation equation for the film yields

$$q = k_l(T_w - T_{int})/\delta. \tag{8}$$

Nomenclature

A = dispersion constant
c_p = specific heat at constant pressure
D = bubble diameter
D_c = cavity diameter
D_d = bubble diameter at departure
$\mathbf{g}$ = gravity vector
H = step function
h = grid spacing for the macro region
h_{ev} = evaporative heat transfer coefficient
h_{fg} = latent heat of evaporation
k = thermal conductivity
l_o = characteristic length, $\sqrt{\sigma/g(\rho_l - \rho_v)}$
M = molecular weight
$\mathbf{m}$ = mass flux vector defined in Eq. (17)
Nu = Nusselt number, $l_o q/k\Delta T$
p = pressure
q = heat flux
R = radius of computational domain
$\bar{R}$ = universal gas constant
R_o = radius of dry region beneath a bubble
R_1 = radial location of the interface at $y = h/2$
r = radial coordinate
T = temperature
ΔT = temperature difference, $T_w - T_{sat}$
t_o = characteristic time, l_o/u_o
u = r-directional velocity
$\mathbf{u}$ = velocity vector, (u, v)
$\mathbf{u}_{int}$ = interfacial velocity vector
u_o = characteristic velocity, $\sqrt{gl_o}$
$\dot{V}_{micro}$ = rate of vapor volume production from the microlayer
ΔV_{micro} = control volume near the micro region
v = y-directional velocity
Y = height of computational domain
y = vertical coordinate
α = thermal diffusivity
β_T = coefficient of thermal expansion
δ = liquid film thickness
δ_T = thermal layer thickness
θ = dimensionless temperature, $(T - T_{sat})/\Delta T$
κ = interfacial curvature
μ = dynamic viscosity
ν = kinematic viscosity
ρ = density
σ = surface tension
σ_T = variation of surface tension with temperature
ϕ = level set function
φ = contact angle

Subscripts

int = interface
l, v = liquid, vapor
r, y, t = $\partial/\partial r$, $\partial/\partial y$, $\partial/\partial t$
sat, w = saturation, wall

The inertial terms in the momentum equation and convection terms in the energy equation can be neglected because the Reynolds number based on the liquid film thickness and the liquid velocity (smaller than 0.05 m/sec for $\Delta T = 8.5$ K) in the micro region is less than unity.

Using a modified Clausis Clayperon equation, (e.g., Wayner, 1992), the evaporative heat flux is written as

$$q = h_{ev}[T_{int} - T_v + (p_l - p_v)T_v/\rho_l h_{fg}] \tag{9}$$

where

$$h_{ev} = 2(M/2\pi\bar{R}T_v)^{0.5}\rho_v h_{fg}^2/T_v; \quad T_v = T_{sat}(p_v). \tag{10}$$

The pressures in the vapor and liquid phases are related (Lay and Dhir, 1995) as

$$p_l = p_v - \sigma\kappa - \frac{A}{\delta^3} + \frac{q^2}{\rho_v h_{fg}^2} \tag{11}$$

where surface tension, σ, is taken to be a function of temperature and A is the dispersion constant relating disjoining pressure to the film thickness. In Eq. (11), the second term on the right-hand side accounts for the capillary pressure, the third term for the disjoining pressure, and the last term originates from the recoil pressure. The curvature of the interface is defined as

$$\kappa = \frac{1}{r}\frac{\partial}{\partial r}\left(r\frac{\partial\delta}{\partial r}\Big/\sqrt{1+\left(\frac{\partial\delta}{\partial r}\right)^2}\right). \tag{12}$$

The combination of the mass, momentum, and energy equations for the microlayer yields

$$\delta'''' = f(\delta, \delta'\delta''\delta''') \tag{13}$$

where $'$ denotes $\partial/\partial r$.

The boundary conditions for the above equation are as follows:

at $r = R_o$,

$$\delta = \delta_o; \quad \delta' = \delta''' = 0 \tag{14}$$

where δ_o is of the order of molecular size (refer to Lay and Dhir (1995)).

at $r = R_1$,

$$\delta = h/2; \quad \delta'' = 0 \tag{15}$$

where $h/2$ is the distance to the first computational node for the level set function, ϕ, from the wall. In implementing the above boundary conditions the radius R_1 was determined from the solution of macro region. For a given dispersion constant, the microlayer formulation, Eq. (13), and R_o are solved with five boundary conditions, Eqs. (14) and (15). In this study an apparent contact angle is defined as

$$\tan\varphi = h/2(R_1 - R_o). \tag{16}$$

Macro Region. For numerically analyzing the macro region, the level set formulation developed by Son and Dhir (1998) for film boiling is used. The interface separating the two phases is captured by ϕ, which is defined as a signed distance from the interface. The negative sign is chosen for the vapor phase and the positive sign for the liquid phase. The momentum and energy equations for the vapor-liquid region are written as

$$\rho\left(\frac{\partial\mathbf{u}}{\partial t} + \mathbf{u}\cdot\nabla\mathbf{u}\right) = -\nabla p + \rho\mathbf{g} - \rho\beta_T(T - T_{sat})\mathbf{g} - \sigma\kappa\nabla H + \nabla\cdot\mu\nabla\mathbf{u} + \nabla\cdot\mu\nabla\mathbf{u}^T$$

$$\rho c_{pl}\left(\frac{\partial T}{\partial t} + \mathbf{u}\cdot\nabla T\right) = \nabla\cdot k\nabla T \quad \text{for } H > 0$$

$$T = T_{sat}(p_v) \quad \text{for } H = 0$$

where

$$\rho = \rho_v + (\rho_l - \rho_v)H$$

$$\mu^{-1} = \mu_v^{-1} + (\mu_l^{-1} - \mu_v^{-1})H$$

$$k^{-1} = k_l^{-1}H$$

$$H = 1 \quad \text{if } \phi \geq +1.5h$$

$$= 0 \quad \text{if } \phi \leq -1.5h$$

$$= 0.5 + \phi/(3h) + \sin[2\pi\phi/(3h)]/(2\pi) \quad \text{if } |\phi| \leq 1.5h$$

where h is a grid spacing. The step function, H, is smoothed over three grid spacings to prevent numerical instability arising from discontinuous material properties (refer to Sussman et al., 1994). The mass conservation equation including the effect of volume expansion due to liquid-vapor phase change is derived from the conditions of the mass continuity and energy balance at the interface:

$$\mathbf{m} = \rho(\mathbf{u}_{int} - \mathbf{u}) = k\nabla T/h_{fg} \tag{17}$$

$$\nabla\cdot\mathbf{u} = -\frac{1}{\rho}\left(\frac{\partial\rho}{\partial t} + \mathbf{u}\cdot\nabla\rho\right) + \dot{V}_{\text{micro}} = \frac{\mathbf{m}}{\rho^2}\cdot\nabla\rho + \dot{V}_{\text{micro}}. \tag{18}$$

In Eq. (18), $\dot{V}_{\text{micro}}$ is obtained from the microlayer solution as

$$\dot{V}_{\text{micro}} = \int_{R_o}^{R_1}\frac{k_l(T_w - T_{\text{int}})}{\rho_v h_{fg}\delta\Delta V_{\text{micro}}}rdr \tag{19}$$

where ΔV_{micro} is a vapor-side control volume near the micro region, which was arbitrarily chosen to be $R_1 - 3h \leq r \leq R_1$ and $0 \leq y \leq h$. In the level set formulation, the level set function, ϕ, is advanced as

$$\frac{\partial\phi}{\partial t} = -\mathbf{u}_{\text{int}}\cdot\nabla\phi \tag{20}$$

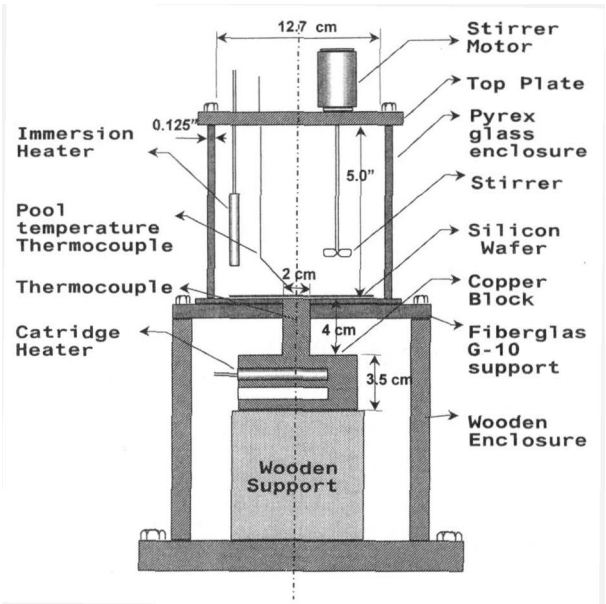

Fig. 2 Experimental setup

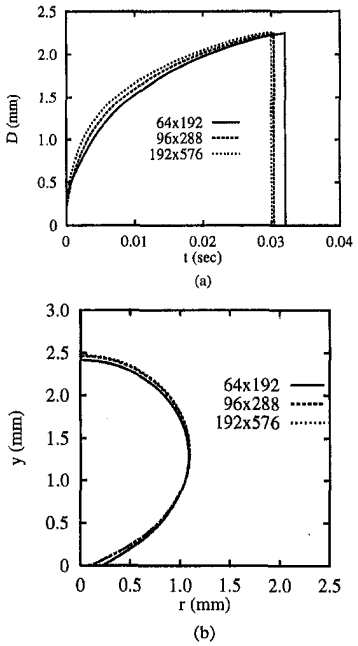

Fig. 3 Effect of mesh size on the numerical results for $\Delta T = 6.2$ K and $A = -8.5 \times 10^{-21}$ J; (*a*) the bubble growth and (*b*) the bubble shape at $t = 0.03$ sec

and is reinitialized as

$$\frac{\partial \phi}{\partial t} = \frac{\phi_o}{\sqrt{\phi_o^2 + h^2}}(1 - |\nabla \phi|) \tag{21}$$

where ϕ_o is a solution of Eq. (20).

The boundary conditions for the governing equations for the macro region are:

at the wall ($y = 0$),

$$u = v = 0,\ T = T_w,\ \phi = -\cos \varphi; \tag{22}$$

at the planes of symmetry ($r = 0, R$),

$$u = \frac{\partial v}{\partial r} = \frac{\partial T}{\partial r} = \frac{\partial \phi}{\partial r} = 0; \tag{23}$$

at the top of computational domain (free surface, $y = Y$),

$$\frac{\partial u}{\partial y} = \frac{\partial v}{\partial y} = \frac{\partial \phi}{\partial y} = 0,\ T = T_{sat}. \tag{24}$$

The procedure used to match asymptotically the solutions for the micro and macro regions is as follows: (i) guess a contact angle, (ii) solve the macro-region equations, (iii) determine R_1 (radial location of the vapor-liquid interface at $y = h/2$), (iv) solve the microlayer formulation with five boundary conditions for a given dispersion constant and determine R_o, (v) obtain the apparent contact angle from Eq. (16), and (vi) repeat steps (i)–(v) if the contact angle obtained in step (v) is different from the guessed value in step (i).

Experiments

In order not to cloud the bubble growth and departure data obtained on a test nucleation site by the activity at spurious cavities surrounding the test site, a single cavity was micromachined at the center of a mirror-polished 100 silicon wafer. The wafer had a diameter of 10 cm and a 10 μm square cavity with a depth of 20 μm was formed in the geometric center of the wafer. The wafer was heated in the central portion with power supplied from a cartridge heater embedded in a copper cylinder having a diameter of 2 cm. The silicon wafer was bonded to the copper block by using Omega Bond (OB-200) conductive adhesive. Four Type K thermocouples were placed in the copper block at a distance of 10 mm apart with the top thermocouple being 2 mm from the upper surface of the copper block. The wafer was supported not only by the copper block, but also by G-10 insulation surrounding the copper block. The test surface was housed in a 15 × 15 × 15 cm cubic chamber. Figure 2 shows the experimental apparatus. The boiling chamber is open at the top, but has stainless steel support for mounting the auxiliary heater, stirrer, and a movable thermocouple to measure the pool temperature.

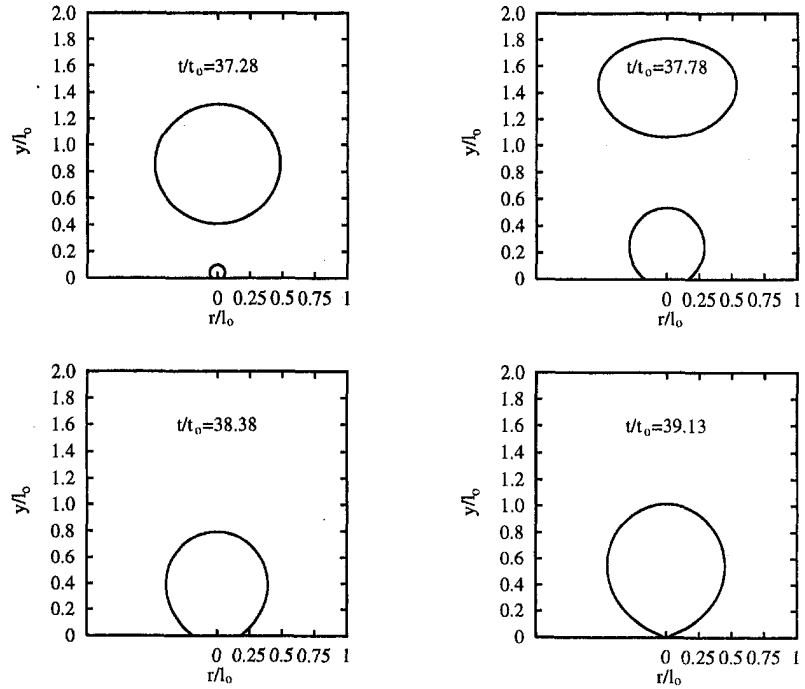

Fig. 4 Bubble growth pattern for $\Delta T = 6.2$ K and $A = -8.5 \times 10^{-21}$ J

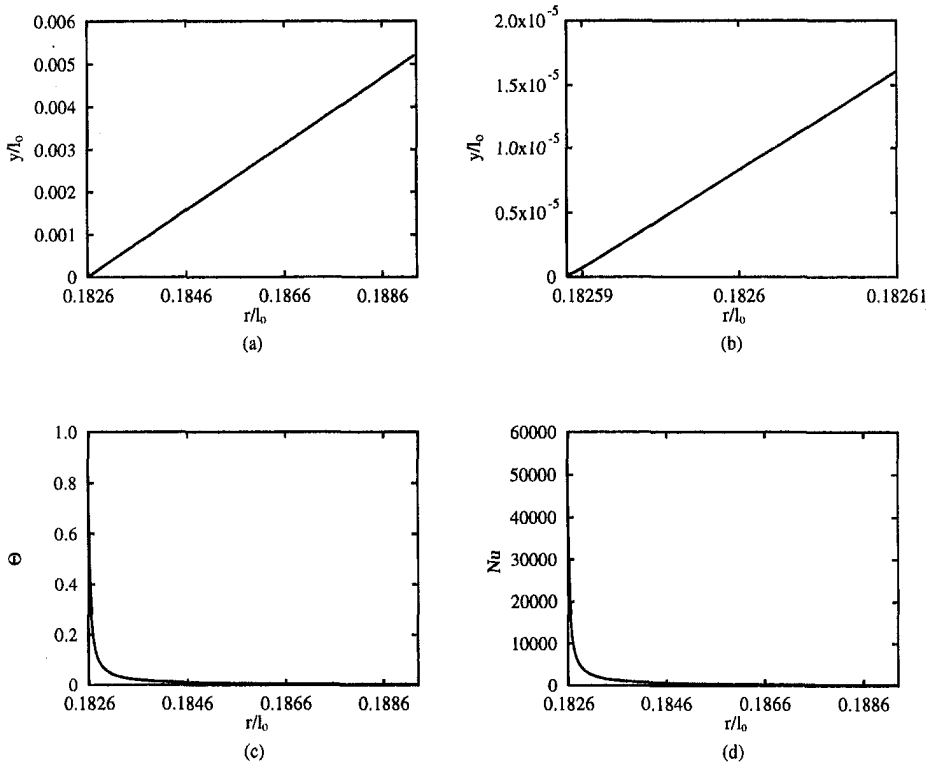

Fig. 5 Results for the micro region at $t/t_o = 38.38$; (*a*) and (*b*) interface shape, (*c*) interfacial temperature, and (*d*) heat transfer coefficient for $\Delta T = 6.2$ K and $A = -8.5 \times 10^{-21}$ (J)

Prior to conducting of the boiling experiments, the test surface was thoroughly cleaned with isopropanol followed by methanol. The surface was then blow-dried and was heated to 100°C to remove any residual film of cleansing agents. A small droplet of the test liquid was placed on the wafer surface and a photograph was taken. From the photograph, a static contact angle of the liquid with the silicon wafer surface was determined. The test liquid (distilled water) was boiled for at least half an hour to remove any dissolved air in the liquid. A calibration for the cumulative thermal resistance of the conductive adhesive layer joining the copper substrate with the wafer and the wafer itself was made. This thermal resistance was used to determine the temperature of the boiling surface as a function of heat flux. The calculated temperature was verified by placing a thermocouple directly on the boiling surface of the silicon wafer exposed to the saturated liquid.

Subsequently, the energy was supplied to the cartridge heater embedded in the copper block and the surface temperature of the silicon wafer was brought to the saturation temperature of water. Preboiled water was poured into the test chamber and auxiliary heater and stirrer were turned on in order to maintain the liquid pool at the saturation temperature. Just prior to recording of the bubble growth and departure data, the power to the auxiliary heater and the stirrer was shut off in order to obtain a quasi-static pool. The bubble growth and departure processes were recorded on a video camera operating at 450 frames per second. At a given time, the data were recorded for several bubble growth and departure cycles.

Results and Discussion

In carrying out numerical simulation, the characteristic length, l_o, the characteristic velocity, u_o, and the characteristic time, t_o, are defined as

$$l_o = \sqrt{\sigma/g(\rho_l - \rho_v)};\ u_o = \sqrt{gl_o};\ t_o = l_o/u_o. \qquad (25)$$

During numerical simulations of partial nucleate boiling, the properties of water at 1 atm. are used. The computation domain is chosen to be $(R/l_o, Y/l_o) = (1, 3)$ so that the bubble growth is not affected by the computational boundary. To initiate the computations, the initial fluid temperature profile is taken to be linear in the natural convection thermal boundary layer and fluid velocity is set equal to zero. The initial thermal boundary layer thickness, δ_T, is evaluated from the correlation for the turbulent natural convective heat transfer (refer to Kays and Crawford, 1980) as

$$\delta_T = 7.14(\nu_l\alpha_l/g\beta_T\Delta T)^{1/3}.$$

Since in reality partial nucleate boiling on a horizontal surface is a cyclic process, the computations should be carried out over several cycles until no cycle-to-cycle change in the bubble growth pattern or in the temperature profile in the thermal boundary layer is observed.

To select an appropriate mesh size, convergence for grid resolutions was tested with mesh points of 64×192, 96×288 and 192×576. The results are plotted in Fig. 3. As the mesh points increase, the relative difference of the bubble growth rates between successive mesh sizes becomes small. For 96×288 and 192×576 meshes, the difference of the bubble growth periods is less than two percent. Also, the bubble shapes at departure for the two finest grids have shown insignificant differences. Therefore, most of computations in this study are performed on 96×288 grid points to save the computing time without losing the accuracy of numerical results. During the computations, time steps were chosen to satisfy the CFL condition, $\Delta t \leq h/(|u| + |v|)$, due to the explicit treatment of the convection terms and the condition that the numerical results should not change if the time steps are halved. An appropriate time step is approximately a dimensionless time of 5×10^{-4}.

Figure 4 shows the bubble growth pattern during one cycle for $\Delta T = 6.17$ K and $A = -8.5 \times 10^{-21}$ J. As mentioned earlier, the solution for the macro region is coupled with the solution for the micro region. The results for the micro region corresponding to the bubble at $t/t_o = 38.38$ are plotted in Fig. 5. The value of the radius of the bubble base, $(r/l_o, y/l_o) = (R_1/l_o, h/2l_o) = (0.189, 0.005)$ at $t/t_o = 38.38$ in Fig. 4, obtained in the macro region

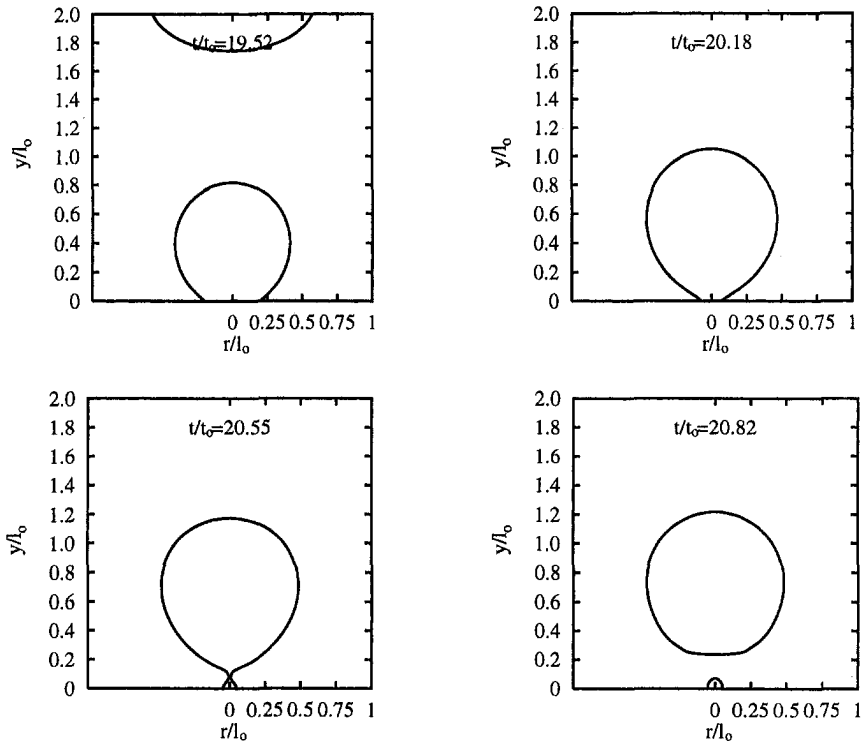

Fig. 6 Bubble growth pattern for $\Delta T = 6.2$ K and $A = -8.5 \times 10^{-21}$ J with a cavity of $D_c = 250$ μm

serves as a boundary condition for the governing equations for the micro region in Fig. 5(*a*). From Fig. 5(*b*), it is seen that due to the contribution of disjoining pressure the slope of the interface decreases to zero rapidly near the nonevaporating region ($\delta = \delta_o$). As the thickness of the liquid microlayer decreases, the interface temperature rises up to the wall temperature as shown in Fig. 5(*c*). Also, significant evaporative heat transfer is observed in the micro region. The apparent contact angle (38 deg from Fig. 5(*a*)) and the total energy removal integrated over the micro region plotted in Fig. 5(*d*) are used in the calculations for the macro region. In the present calculations, for a given dispersion constant (A), the apparent contact angle is nearly independent of the bubble growth process. In reality, however, the dynamic contact angles (advancing and receding contact angles) differ from the static contact angle. The hysteresis of contact angle on a real solid surface is not modeled in this study and this may have some effect on the shape of the vapor-liquid interface at the heated surface during bubble departure.

It is seen from Fig. 4 that during the early period of bubble growth ($37.28 < t/t_o < 38.38$), the location where the vapor-liquid interface contacts the solid wall moves radially outwards. However, the horizontal movement of the bubble base is retarded by the wall friction and the surface tension forcing the bubble shape to satisfy the geometric condition (contact angle). This in turn tends to push the upper portion of the bubble outwards and as a result leads to increased buoyancy force. The nonuniform bubble motion induces a clockwise vortex in the liquid layer. When liquid vortex becomes stronger with the increase of the bubble diameter, the bubble base moves inwards ($38.38 < t/t_o < 39.13$). The departure process occurs rapidly because the dominance of buoyancy over surface tension accelerates as the bubble base shrinks. According to the experimental observation of Siegel and Keshock (1964) for the bubble departure process, the bubble neck forms near the wall and thereafter the bubble breaks off. The small vapor portion left after the bubble departure serves as a nucleus for the next bubble. This condition can be achieved through the simulation of the bubble growth with a cavity of $D_c = 250$ μm as demonstrated in Fig. 6. The computation are performed with grid points of 128×384. Also, to satisfy the condition that the bubble base can not shrink beyond the cavity mouth at $t/t_o = 20.18$ and $t/t_o = 20.55$ in Fig. 6, an additional constraint is imposed for evaluation of the level set function at the wall:

$$\phi \leq 0 \qquad \text{for } r \leq D_c/2. \tag{26}$$

In Fig. 6 the numerical simulation including a cavity shows clearly the departure process that is consistent with the experimental observation of Siegel and Keshock (1964). However, the cavities existing on a real surface are one or two orders of magnitude smaller than the cavity used in this computation, $D_c = 250$ μm. For an extremely small cavity, the cavity does not affect the overall

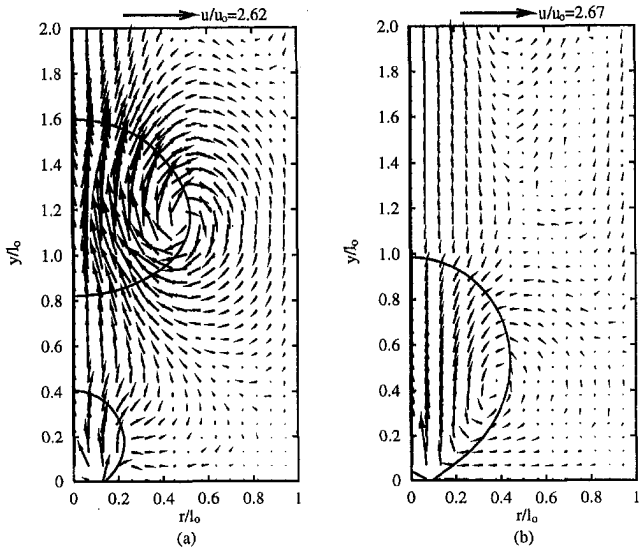

Fig. 7 Flow patterns during growth and detachment of single bubbles for $\Delta T - 6.2$ K and $A = -8.5 \times 10^{-21}$ J; (*a*) $t/t_o = 37.58$ and (*b*) $t/t_o = 39.03$

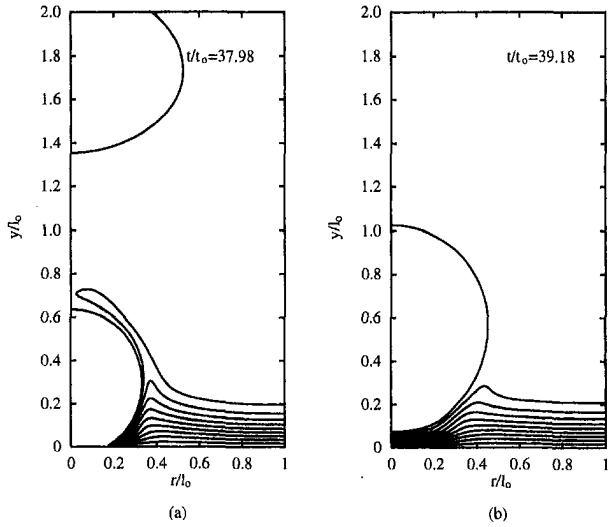

Fig. 8 Temperature fields with temperature interval of 0.62 K for ΔT = 6.2 K and $A = -8.5 \times 10^{-21}$ J

bubble growth because the breakoff period of a bubble is very short compared with the overall bubble growth period. As such the effect of cavity on the bubble growth is not included in most of computations of the present study and the small bubble serving as nucleus for the next cycle is placed on the surface after the previous bubble departs (at t/t_o = 37.28 in Fig. 4). The initial bubble size chosen in the present computations is small enough to have no significant effect on the overall bubble growth. The waiting periods for the cavity considered in the present work are practically zero because the wall temperature is assumed to remain constant. In the experiment with a constant heat flux condition, the wall temperature decreases when the cold pool liquid fills the area vacated by the departing bubble. The liquid layer and the heater surface have to be heated to a temperature necessary to initiate the next bubble. Such a waiting period can be predicted when a conjugate problem involving conduction in the solid is solved simultaneously. In the present computations the waiting period was chosen so that a growing bubble was not disturbed by the previously departed bubble.

The flow field in and around a bubble growing on the wall and for a detached bubble is shown in Fig. 7(*a*). During the early period of bubble growth, the liquid around the bubble is seen to be pushed out. A circulatory flow pattern inside the bubble as well as in the liquid outside is clearly seen for the freely rising detached bubble. The vapor velocity vectors in the bubble are reflective of the bulk movement of the bubble in the upward direction and the changes in the bubble shape as the bubble rises in the pool. There is no inflow or outflow of vapor at the vapor-liquid interface. Figure 7(*b*) shows the flow pattern in and around the bubble shortly before detachment. On the upper portion of the bubble, the

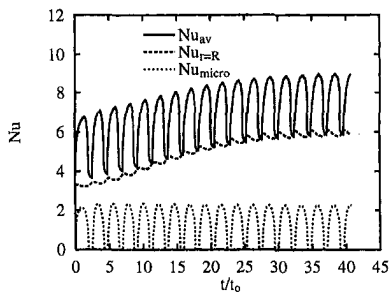

Fig. 9 Variation of Nusselt number with time for various bubble growth cycles for ΔT = 6.2 K and $A = -8.5 \times 10^{-21}$ J

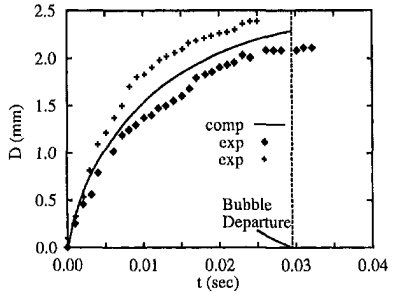

Fig. 10 Comparison of bubble diameter predicted from numerical simulation with experimental data obtained by Siegel and Keshock (1964) for ΔT = 6.2 K and φ = 38 deg ($A = -8.5 \times 10^{-21}$ J)

liquid is being pushed outwards whereas the liquid flow is radially inward in the lower portion of the bubble. The temperature field around the bubble is shown in Fig. 8. The crowding of the isotherms underneath the bubble is reflective of the very high heat flux in that region. Initially when a bubble locates inside the thermal boundary layer, the bubble grows as a result of evaporation all around of the bubble interface including the micro region. As the bubble grows out of the thermal layer, the energy required for evaporation is supplied through only the portion around the bubble base. Also it is seen from Fig. 8(*b*) that just after bubble detachment a thin thermal layer forms on the area vacated by the departing bubble and the thickness of the thermal layer increases with time due to transient thermal conduction.

Figure 9 shows temporal variation of predicted Nusselt number based on the area averaged heat flux at the wall, Nu_{av}, and the local Nusselt number at the edge of the domain, $Nu_{r=R}$. Because of the uncertainty in the specification of the initial condition, magnitude of Nusselt number is seen to change from cycle to cycle. However, after about 14 cycles, the steady-state condition appears to have been achieved. Nu_{micro} is the Nusselt number based on the contribution of microlayer. It is seen that for this set of calculations the microlayer contributes about 20 percent to the total flux. Also, it is noted that local heat transfer at $r = R$ is 80 percent higher than that obtained from the correlation for the turbulent natural convection. This indicates that the liquid vortex associated with a growing and departing bubble is much stronger than the motion induced by pure natural convection.

In Fig. 10 a comparison of the bubble growth predicted from the numerical calculations is made with the data reported by Seigel and Keshock (1964) for ΔT = 6.2 K and φ = 38 deg. The numerical predictions are bounded by the upper and lower limits of the data. The model also predicts correctly the bubble diameter at departure and time for departure.

A similar comparison of the predictions of the bubble diameter as a function of time is made in Fig. 11 and 12 with the data obtained from the present experiments. The data and predictions

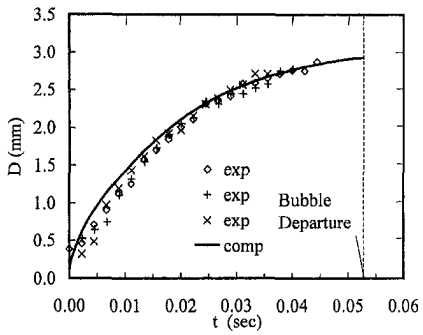

Fig. 11 Comparison of bubble diameter predicted from numerical simulation with experimental data for ΔT = 7.0 K and φ = 50 deg ($A = -14.4 \times 10^{-21}$ J)

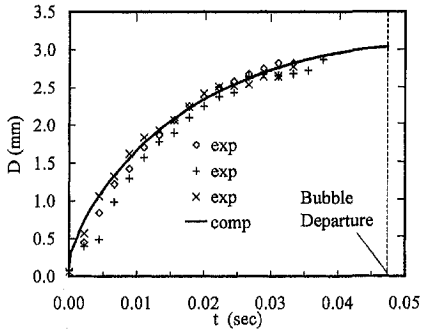

Fig. 12 Comparison of bubble diameter predicted from numerical simulation with experimental data for ΔT = 8.5 K and φ = 50 deg (A = -14.4×10^{-21} J)

plotted in Fig. 11 and 12 are for saturated water at one atmosphere pressure and for wall superheats of 7 K and 8.5 K, respectively. The static contact angle for water on silicon wafer was found to be 50 deg. The advancing and receding contact angles during bubble growth were also measured (Ramanujapu and Dhir (1998)) and found to vary between ±5 deg of the static value. In making the predictions, plotted in Fig. 11 and 12, the contact angle was kept constant at 50 deg. Different values of the contact angle were obtained by changing the value of A. Thus a proportionality relationship was developed between the dispersion constant and the contact angle. For both superheats the predictions of bubble growth, bubble diameter at departure and bubble growth time are found to be in good agreement with the data except that model generally tends to overpredict the growth period. In Fig. 13 the bubble shape just prior to departure, obtained from the usual observations for a superheat of 8.5 K is compared with that obtained from numerical simulation. Overall the agreement between the two is quite good. However, slight differences are observed in the neck region.

The dependence of bubble growth on surface wettability is plotted in Fig. 14. Computations were made for three different contact angles (φ) of 25 deg, 30 deg, and 38 deg which correspond to dispersion constants of -3×10^{-21} (J), -5×10^{-21} (J) and -8.5×10^{-21} (J). It is seen from Fig. 14 that as the contact angle increases, the bubble growth period increases. Also, the bubble diameter at departure becomes larger as the contact angle increases. This is caused by the fact that as the contribution of surface tension increases with increase in the contact angle, the vapor volume required for bubble departure also increases. The increase of bubble departure diameter with contact angle is found to be generally in agreement with the correlations proposed by Fritz (1935) and Staniszewski (1959).

Figure 15 shows the effect of wall superheat on the bubble growth. The bubble diameter at departure and the bubble growth period are listed in Table 1. With increase in wall superheat vapor production rate increases. As a result the growth period decreases

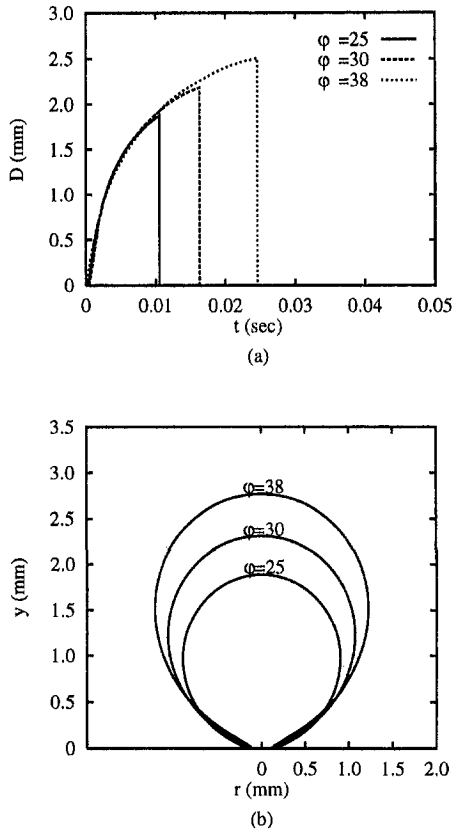

Fig. 14 Effect of contact angle (φ) on bubble growth; (*a*) variation of bubble diameter with time and (*b*) bubble shape at departure for ΔT = 8.5 K

from 29.5 msec to 20.5 msec when ΔT is increased from 6.2 K to 12.5 K. Also, the bubble diameter at departure increases with wall superheat. This indicates that for a fixed contact angle, the bubble diameter at departure depends on the growth rate (bubble dynamics) which increases with wall superheat.

Nusselt numbers based on heat transfer coefficient averaged over the cell area are plotted in Fig. 16. During early period of bubble growth, the Nusselt number increases because the area of the microlayer increases as the bubble base expands. Thereafter, the Nusselt number decreases during a bubble departure period. Also, it is seen from Fig. 16 that as the wall superheat increases the Nusselt number increases. This is caused by the fact that the bubble growth rate increases with ΔT and this in turn induces a stronger vortex motion. The time and area-averaged Nusselt numbers are listed in Table 1. The Nusselt numbers and heat fluxes for the partial nucleate boiling on a single nucleation site vary as $\Delta T^{0.4}$ and $\Delta T^{1.4}$ respectively. However, on a real surface with various sizes of cavities, the heat fluxes vary much steeply with ΔT

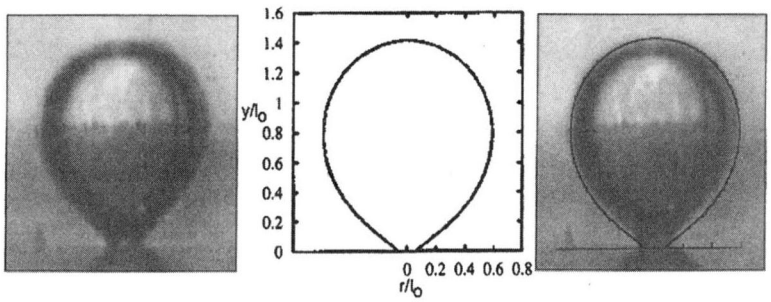

Fig. 13 Comparison of prediction of bubble shape at departure with data for ΔT = 8.5 K and φ = 50 deg

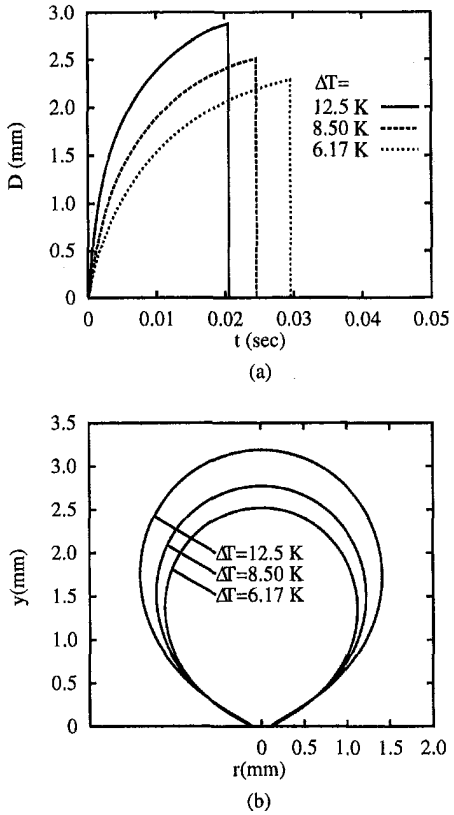

Fig. 15 Effect of wall superheat (ΔT) on bubble growth; (*a*) variation of bubble diameter with time and (*b*) bubble shape at departure for φ = 38 deg

because the number density of active sites strongly depends on the wall superheat. To predict nucleate boiling heat flux values on a real surface, the effect of cavity number density should be included in the numerical model. This can be achieved from the numerical simulation of a single bubble on an effective surface area corresponding to the number density of cavities on a real surface, which will be done in the future.

Conclusions

1 A numerical simulation of a growing and departing bubble on a horizontal surface has been carried out without any approximation of the bubble shape. The effect of microlayer evaporation is included in the analysis.

Table 1 Predicted bubble growth and heat transfer rate for different wall superheat for φ = 38 deg

ΔT (K)	D_d (mm)	Growth period (msec)	Nu	q (W/cm^2)
6.2	2.28	29.5	7.86	1.32
8.50	2.51	24.6	8.83	2.04
12.5	2.88	20.5	10.4	3.54

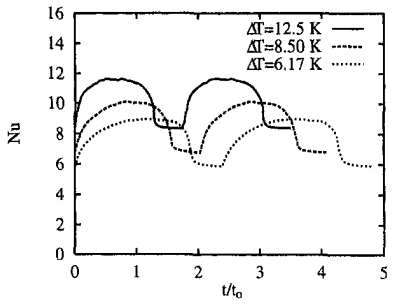

Fig. 16 Effect of wall superheat (ΔT) on Nusselt number for φ = 38 deg

2 From the numerical simulation, the location where the vapor-liquid interface contacts the wall is observed to move outwards and then inwards as the bubble grows and departs.

3 The local wall heat flux is seen to vary cyclically during the bubble growth. The contribution of microlayer to the total heat flux is found to be about 20 percent.

4 The departing bubble becomes larger with the increase in contact angle and wall superheat. The bubble growth scenario predicted from numerical analysis compares well with that observed in the experiments.

Acknowledgment

This work received support from NASA Microgravity Fluid Physics Program.

References

Cooper, M. G., and Lloyd, A. J. P., 1969, "The Microlayer in Nucleate Pool Boiling," *Int. J. Heat Mass Transfer,* Vol. 12, pp. 895–913.

Fritz, W., 1935, "Maximum Volume of Vapor Bubbles," *Physik Zeitschr.,* Vol. 36, pp. 379–384.

Hsu, Y. Y., and Graham, R. W., 1976, *Transport Processing in Boiling and Two Phase Systems,* Hemisphere, Washington, DC.

Kays, W. M., and Crawford, M. E., 1980, *Convective Heat and Mass Transfer,* McGraw-Hill, New York, p. 328.

Lay, J. H., and Dhir, V. K., 1995, "Shape of a Vapor Stem During Nucleate Boiling of Saturated Liquids," ASME JOURNAL OF HEAT TRANSFER, Vol. 117, pp. 394–401.

Lee, R. C., and Nydahl, J. E., 1989, "Numerical Calculation of Bubble Growth in Nucleate Boiling From Inception Through Departure," *ASME Journal of Heat Transfer*, Vol. 111, pp. 474–479.

Mikic, B. B., Rohsenow, W. M., and Griffith, P., 1970, "On Bubble Growth Rates," *Int. J. Heat Mass Transfer,* Vol. 13, pp. 647–666.

Plesset, M. S., and Zwick, S. A., 1954, "Growth of Vapor Bubbles in Superheated Liquids," *J. Appl. Phys.,* Vol. 25, pp. 493–500.

Ramanujapu, N., and Dhir, V. K., 1999, "Dynamics of Contact Angle During Growth and Detachment of a Vapor Bubble at a Single Nucleation Site," presented at ASME-JSME Conference in San Diego, CA.

Siegel, R., and Keshock, E. G., 1964, "Effects of Reduced Gravity on Nucleate Boiling Bubble Dynamics in Saturated Water," *AICHE Journal,* Vol. 10, pp. 509–517.

Son, G., and Dhir, V. K., 1998, "Numerical Analysis of Film Boiling Near Critical Pressure With a Level Set Method," ASME JOURNAL OF HEAT TRANSFER, Vol. 120, pp. 183–192.

Staniszewski, B. E., 1959, "Nucleate Boiling Bubble Growth and Departure," Technical Report No. 16, Division of Sponsored Research, Massachusetts Institute of Technology, Cambridge, MA.

Sussman, M., Smereka, P., and Osher, S., 1994, "A Level Set Approach for Computing Solutions to Incompressible Two-Phase Flow," *J. of Comput. Phys.,* Vol. 114, pp. 146–159.

Wayner, P. C., Jr., 1992, "Evaporation and Stress in the Contact Line Region," *Proceedings of the Engineering Foundation Conference on Pool and External Flow Boiling,* V. K. Dhir and A. E. Bergles, eds., Santa Barbara, CA, pp. 251–256.